

Kinematics of the Local Spiral Structure Revealed by Young Stars in *Gaia* DR3

DEJIAN LIU,^{1,2} YE XU,^{1,2} CHAOJIE HAO,^{1,2} SHUAIBO BIAN,¹ ZEHAO LIN,^{1,2} YINGJIE LI,¹ AND JINGJING LI¹

¹*Purple Mountain Observatory, Chinese Academy of Sciences, Nanjing 210023, People's Republic of China*

²*School of Astronomy and Space Science, University of Science and Technology of China, Hefei 230026, People's Republic of China*

ABSTRACT

Using young open clusters and O–B2-type stars in *Gaia* DR3, we investigate the kinematics of the local spiral structure. In general, the young sources in the outer spiral arms may present larger peculiar motions than those in the inner spiral arms. The young open clusters appear to have smaller peculiar motions than the O–B2-type stars, and the sources in both the Perseus and Local Arms may show an inward motion toward the Galactic center and rotate slower than Galactic rotation. Meanwhile, the sources in the Carina Arm may move in the opposite direction from the Sun to the Galactic center and rotate marginally faster than Galactic rotation. In addition, using young open clusters and O–B2-type stars, we have improved the distance estimations of kinematic methods for several regions near the Sun.

Keywords: Galaxy kinematics (602); Open star clusters (1160); OB stars (1141)

1. INTRODUCTION

The kinematics of the spiral arms of the Milky Way are of great interests to astronomers, as they can help unveil the formation and evolution of our home Galaxy. As key elements of the spiral arms, the measurements and analysis of the spatial distributions, velocities, and rotational orbits of stars and gas therein can provide valuable insights into Galactic structure and dynamics (Binney & Tremaine 2008), as well as the gravitational potential of the Milky Way (Sakai et al. 2019; Immer et al. 2019).

Numerous young objects have been used to trace the spiral-arm structure of our Galaxy, e.g., high-mass star-formation region (HMSFR) masers yielded by the Bar and Spiral Structure Legacy (BeSSeL) Survey (Brunthaler et al. 2011; Reid et al. 2014, 2019) and the Very Long Baseline Interferometry (VLBI) Exploration of Radio Astrometry (VERA) array (VERA Collaboration et al. 2020), as well as observations of young massive O–B-type stars (Xu et al. 2018, 2021), HII regions (Georgelin & Georgelin 1976; Hou & Han 2014), young open clusters (YOCs, Dias et al. 2019; Hao et al. 2021; Gaia Collaboration et al. 2022a), etc. Although the global Galactic spiral structure is still a topic of debate, the spiral structure within about 5 kpc of the Sun is better understood. There are three spiral segments in the solar neighborhood, namely the Sagittarius–Carina, Local, and Perseus Arms (Reid et al. 2019). Recently, Xu et al. (2023) reconsidered the spiral structure of the Milky Way and proposed that the Sagittarius Arm may be not connected to the Carina Arm. Due to a lack of available sources in the Sagittarius Arm, in this work, we mainly concentrate on the three distinct spiral-arm segments in the solar neighborhood: the Carina, Local, and Perseus Arms.

The kinematics of the Milky Way are closely related to its structure. In recent years, substantial progress in studying the local kinematics using stars provided by *Gaia* and VLBI masers has been achieved. Using *Gaia* data release 2 (Gaia Collaboration et al. 2018a), Gaia Collaboration et al. (2018b) looked at the kinematics of the Milky Way disk, within a radius of several kiloparsecs around the Sun, and found rich and complex kinematics of the Galactic disk and streaming motions in all three dimensional velocity components. Gaia Collaboration et al. (2022a) studied the Galactic spiral structure and kinematics using young stellar populations in *Gaia* data release 3 (DR3, Gaia Collaboration et al. 2022b), and revealed that the velocity field of the OB stars shows streaming motions whose characteristic length is similar to the spiral arm density. As reviewed by Immer & Røgl (2022), based on VLBI masers, researchers have studied the kinematics of sources located in different spiral arm segments. However, many of these studies focused only on the peculiar motion of masers in individual spiral arm segments, while systematic kinematic studies of the local spiral structure, especially using young sources located in the spiral arms, are still very lacking. In this work, based on the

spiral-arm model proposed by Xu et al. (2023), we aim to study the kinematics of the local spiral structure using young stars.

Accurate trigonometric parallaxes and proper motions of HMSFR masers in the northern hemisphere sky have been determined (e.g., Reid et al. 2019; Xu et al. 2021; Bian et al. 2022). The high-precision six-dimensional (6D; 3D spatial and 3D velocity) astrometric parameters of OB stars and YOCs, provided by *Gaia* DR3, enable us to investigate the kinematics of young stars in the local spiral structure, and compare them with those of HMSFR masers. Additionally, based on the astrometric parameters of young stars in the solar neighborhood, we try to provide valuable indications for future distance estimation using kinematic methods.

2. DATA

2.1. YOCs

Xu et al. (2023) compiled a sample that contains more than 5 000 open clusters (OCs) from three catalogs (Hao et al. 2021, 2022b; Castro-Ginard et al. 2022). In this work, we increase this catalog by considering the 38 newly reported OCs by Hao et al. (2022a) and the 101 newly reported OCs by Qin et al. (2023). We also identify potentially duplicate OCs. If the difference between the mean parameters of two OCs are within $3\sigma_i$ ($i = \alpha, \delta, \varpi, \mu_\alpha \cos \delta, \mu_\delta$) in five-dimensional parametric space, they can be regarded as duplicate objects, and we confirm them via visual inspection. After this step, 4 871 OCs remain (see Table 1), of which 3 794 have *Gaia* radial velocity measurement. In the following analysis, we only use young OCs (age < 20 Myr) with parallax accuracies better than 20% and radial velocity uncertainties smaller than 10 km s^{-1} . Determination of the radial velocity uncertainties of OCs is conducted following the same method as Soubiran et al. (2018). Finally, we obtain a sample containing 285 YOCs, and their astrometric parameters are taken from *Gaia* DR3. We perform a parallax zero-point correction for the member stars of each OC (Lindgren et al. 2021), and then use the average parallax of all members as the OC’s parallax.

Table 1. Summary of the Mean Parameters of the Cluster Sample

cluster	N	α (deg)	δ (deg)	ϖ (mas)	σ_ϖ (mas)	$\mu_\alpha \cos \delta$ (mas yr $^{-1}$)	$\sigma_{\mu_\alpha \cos \delta}$ (mas yr $^{-1}$)	μ_δ (mas yr $^{-1}$)	σ_{μ_δ} (mas yr $^{-1}$)	v_{los} (km s $^{-1}$)	$\sigma_{v_{\text{los}}}$ (km s $^{-1}$)	$N_{v_{\text{los}}}$	$\log t$	Ref
UBC1194	64	0.020	63.900	0.330	0.023	-2.496	0.024	-1.261	0.023	-77.9	10.7	5	7.78	Castro2022
Berkeley_58	115	0.063	60.937	0.331	0.084	-3.361	0.091	-1.705	0.089	-4.1	10.0	1	8.47	Scholz2015
NGC_7801	33	0.077	50.711	0.444	0.064	-3.642	0.056	-2.439	0.075	-12.5	14.4	4	9.26	Scholz2015
...														

NOTE—This table is available in its entirety in machine-readable form.

2.2. O–B2-type Stars

We adopt the method of Xu et al. (2023) to identify O–B2-type stars in *Gaia* DR3 and a renormalized unit weight error (**ruwe**) < 1.4 (Lindgren et al. 2021) is used to remove objects with unreliable astrometric solutions. After that, 1 135 O–B2-type stars with *Gaia* radial velocities are selected (see Table 2). The values of the parameter **ipd_gof_harmonic_amplitude** above 0.1 in combination with **ruwe** being larger than 1.4 are indicative of resolved binaries, which are still not correctly handled in the astrometric processing, and may cause spurious solutions (Gaia Collaboration et al. 2021). Hence, these two parameters are adopted to reduce the number of potential binaries, and then reduce the effect due to them, i.e., **ipd_gof_harmonic_amplitude** < 0.1 and **ruwe** < 1.4 (Fabricius et al. 2021). Applying the same criteria of a parallax precision better than 20% and a radial velocity error smaller than 10 km s^{-1} , we obtained a final sample of 300 O–B2-type stars. Same as the OCs, we also perform a parallax zero-point correction for each O–B2-type star in the sample (Lindgren et al. 2021).

3. KINEMATICS OF YOUNG OBJECTS

Using the parallaxes to convert proper motions to linear velocities and combining them with the radial velocities, we derive the peculiar motions (U_s, V_s , and W_s) of the YOCs and O–B2-type stars, using the same method as Reid et al. (2009). U_s, V_s , and W_s are the velocity components towards the Galactic center (GC, radial), in the direction of Galactic rotation (azimuthal), and towards the north Galactic pole, respectively. In the above calculation, the

Table 2. Summary of the Parameters of the O–B2-type Stars

<i>Gaia</i> DR3 ID	α (deg)	δ (deg)	ϖ (mas)	$\sigma\varpi$ (mas)	$\mu_\alpha \cos \delta$ (mas yr $^{-1}$)	$\sigma\mu_\alpha \cos \delta$ (mas yr $^{-1}$)	μ_δ (mas yr $^{-1}$)	$\sigma\mu_\delta$ (mas yr $^{-1}$)	v_{los} (km s $^{-1}$)	σv_{los} (km s $^{-1}$)	T_{eff} (K)
528594342521399168	0.4453	67.5070	1.010	0.012	-1.566	0.011	-1.795	0.012	-42.7	19.3	42190
429366957178085376	1.0123	60.8458	0.303	0.023	-2.544	0.018	-1.969	0.021	-51.0	34.9	24480
431544127639952384	1.9834	63.3354	0.427	0.018	-2.823	0.021	-0.925	0.020	-55.5	6.9	20000
...											

NOTE—This table is available in its entirety in machine-readable form.

fundamental parameters of the Milky Way, $R_0 = 8.15$ kpc, $\Theta_0 = 236$ km s $^{-1}$, and solar motions of $U_\odot = 10.6$ km s $^{-1}$, $V_\odot = 10.7$ km s $^{-1}$, and $W_\odot = 7.6$ km s $^{-1}$ (Reid et al. 2009) are adopted. Meanwhile, a universal rotation curve (Persic et al. 1996) consisting of two parameters, $a_2 = 0.96$ and $a_3 = 1.62$ (Reid et al. 2019), is assumed.

Figure 1 displays the peculiar motions of the YOCs and O–B2-type stars in the Galactic plane, which are almost concordant with each other. There are two significant kinematic features of sources in the Perseus and Local Arms. Near the direction of $l \sim 100^\circ$ – 135° , the YOCs and O–B2-type stars in the Perseus Arm exhibit large peculiar motions, which is consistent with the result shown using HMSFR masers (Reid et al. 2019). Around the direction of $l \sim 70^\circ$ – 90° , both the YOCs and O–B2-type stars in the Local Arm exhibit opposite motions with respect to Galactic rotation, similar to the results of HMSFR masers (Xu et al. 2013). Therefore, these results suggest that the peculiar motions of the different young populations in the solar neighborhood probably are comparable.

To address the issue of whether there are kinematic differences between young stars in different evolutionary stages, we divide the O–B2-type stars into the O-type stars and B0–B2-type stars based on their effective temperature, where the O-type stars are hotter than 30 000 K and B0–B2-type stars are hotter than 20 000 K but colder than 30 000 K (Chen et al. 2013). As shown in Figure 2, we present the peculiar motions of the O- and B0–B2-type stars in the Galactic plane. It appears that the B0–B2-type stars, overall, possess larger peculiar motions than those of the O-type stars.

Next, we investigate the kinematic characteristics of the YOCs and O–B2-type stars in each spiral arm near the Sun, and analyze the average peculiar motion (\overline{U}_s , \overline{V}_s , and \overline{W}_s) of those sources with respect to the Galactocentric radius R . Following Reid et al. (2019), we define an outlier as having greater than a 3σ residual in any peculiar motion component and, based on this, we remove 20 YOCs and 44 O–B2-type stars from the following analysis.

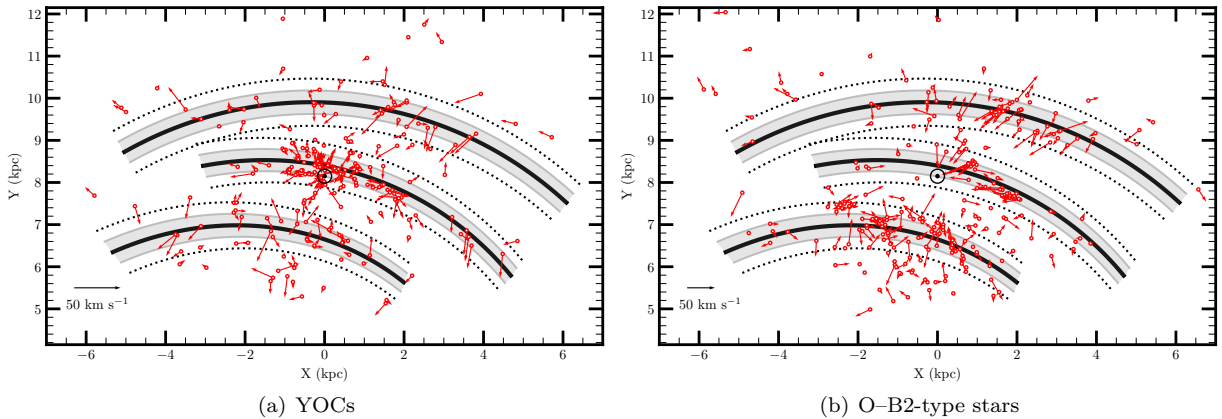


Figure 1. Peculiar motions of the YOCs (left) and O–B2-type stars (right) in the Galactic plane. The parallax uncertainties are smaller than 20% and the radial velocity uncertainties are smaller than 10 km s $^{-1}$. The solid curved lines trace the centers of the spiral arms: from top to bottom are the Perseus, Local, and Carina Arms, respectively (Xu et al. 2023). The shadows and dashed lines are the 1σ and 2σ widths from the center of the spiral arms, respectively. The Sun (black Sun symbol) is at (0, 8.15) kpc (Reid et al. 2019). A 50 km s $^{-1}$ scale vector is shown in the lower-left corner.

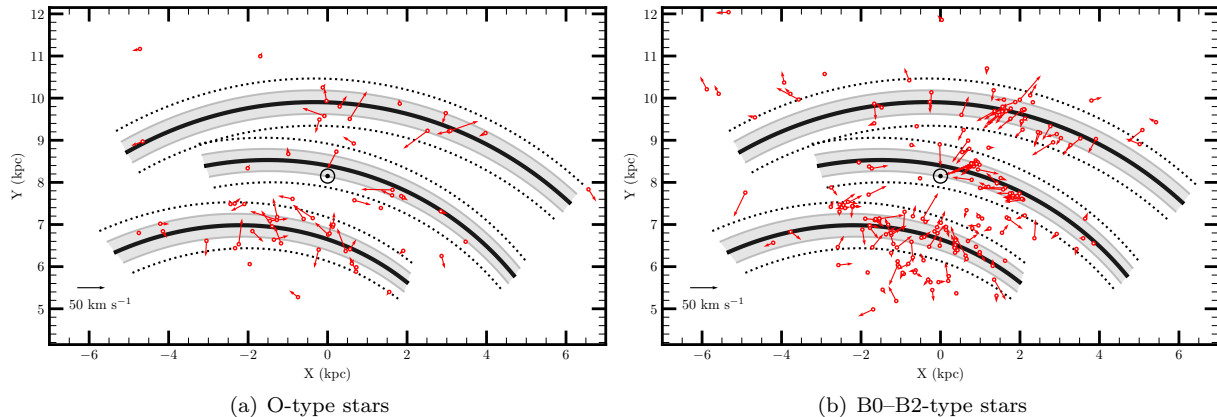


Figure 2. Peculiar motions of the O (left) and B0–B2 (right) stars in Galactic plane. The others features are the same as in Figure 1.

3.1. Kinematics of Young Objects in the Spiral Arms

In this work, we focus on analyzing the kinematic characteristics of sources in the three spiral arms near the Sun, including the Perseus, Local, and Carina Arms. Besides, by comparing the kinematics of sources at different distances (i.e., 1σ and 2σ) from the center of each spiral arms, we can investigate the areas most influenced by the gravitational force of each spiral arms. Adopting the spiral-arm model proposed by Xu et al. (2023), the average peculiar motions and std values are similar for sources located within 1σ and 2σ widths from the center of each spiral arm, so we just use the 2σ for this study. In Figures 3 and 4, we show histograms of peculiar motions of YOCs and O–B2-type stars. Then, we calculate the average peculiar motions and corresponding errors, and the standard deviation (std) of the peculiar motions of sources in each spiral arm, which are listed in Tables 3 and 4. For the 199 HMSFR masers summarized by Reid et al. (2019), and the five newly reported by Xu et al. (2021) and Bian et al. (2022), Xu et al. (2023) re-assigned them to the spiral arms in their new proposed spiral-arm model. Here, the masers belonging to the Perseus Arm in the second and third quadrants, the Local Arm, and the Carina Arm are selected and their average peculiar motions are calculated and compared with those of the YOCs and O–B2-type stars, as listed in Tables 3 and 4. Due to the limited number of samples, the average peculiar motions from Table 3 are not significant at a 3σ level, but they still reflect the potential kinematic characteristics of young objects located in the spiral arms.

As shown in Figure 1, in the Perseus Arm, 18 YOCs and 40 O–B2-type stars are located in the second quadrant, and 13 YOCs and 11 O–B2-type stars are located in the third quadrant. This distribution is consistent with the fact that there are fewer and generally faint clouds in the third quadrant of the Perseus Arm (Dame et al. 2001). 75% YOCs and 73% O–B2-type stars have positive values for the U_s component, and 81% YOCs and 76% O–B2-type stars have negative values for the V_s component. As listed in Table 3, the YOCs and O–B2-type stars in the Perseus Arm have positive average values of the U_s component and negative average values of the V_s component, indicating that the young objects are likely to have a tendency to move towards the GC and move slower than Galactic rotation. It is in line with the previous result obtained from masers (Sakai et al. 2019; Zhang et al. 2019). Besides, on average, the O–B2-type stars may exhibit larger peculiar motions than the masers and YOCs. When separating the O- and B0–B2-type stars, we discover that the U_s and V_s components of the peculiar motions of the O-type stars may be smaller than those of the B0–B2-type stars, while the uncertainties of O-type stars are large.

In the Local arm, 64 YOCs and 44 O–B2-type stars are located in the second quadrant, and 76 YOCs and 8 O–B2-type stars in the third quadrant. 57% YOCs and 75% O–B2-type stars have positive values for the U_s component, 53% YOCs and 71% O–B2-type stars have negative values for the V_s component. Combining with the average peculiar motions of young objects (listed in Table 3), it is likely that O–B2-type stars, on average, present a movement toward the GC and a lagging motion with respect to the Galactic rotation. YOCs may have the same kinematic features as O–B2-type stars, but they are not significant. The sources in the Local Arm may have smaller motions toward the GC than those of sources in the Perseus Arm. The average peculiar motions of the masers in the Local Arm may be larger than those of the YOCs, but smaller than those of the O–B2-type stars in the V_s component. The B0–B2-type stars seem to present larger peculiar motions than the O-type stars.

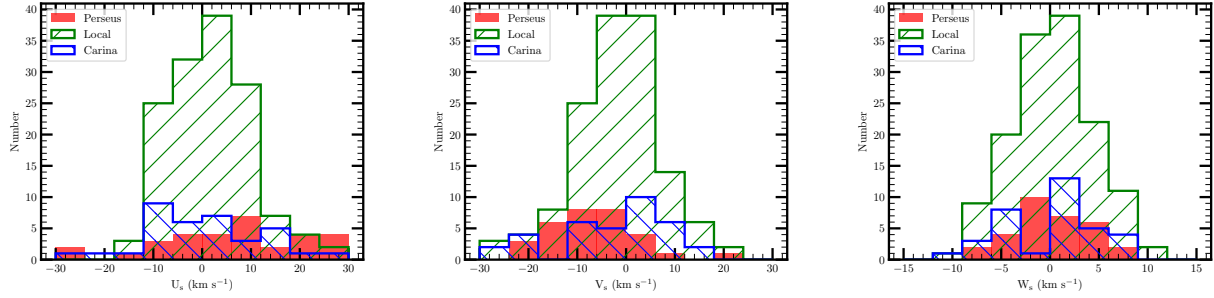


Figure 3. Histograms of peculiar motions of the YOCs.

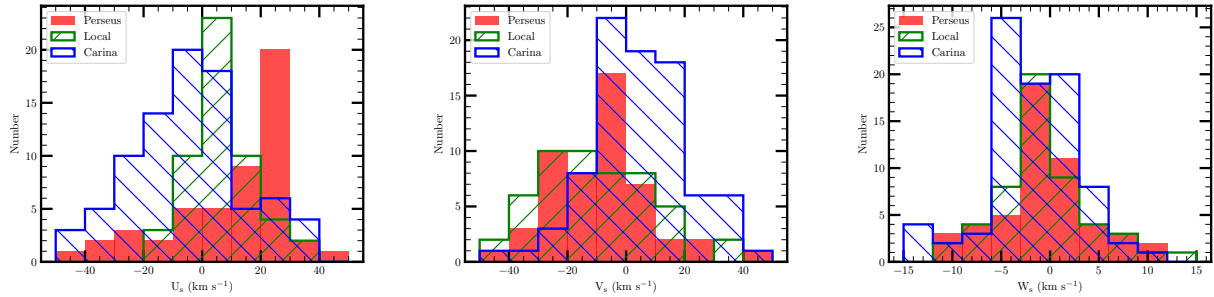


Figure 4. Histograms of peculiar motions of the O–B2 type stars.

In the Carina arm, 51% YOCs and 61% O–B2-type stars have negative values of the U_s component, 51% YOCs and 59% O–B2-type stars have positive values of the V_s component. The O–B2-type stars in the Carina Arm may have different kinematic features, in that they appear to be moving towards the Galactic anticenter. The O–B2-type stars appear to have no lagging motion and may even be ahead of Galactic rotation. The average values for the U_s and V_s components are $0.3 \pm 2.0 \text{ km s}^{-1}$ and $-2.3 \pm 1.9 \text{ km s}^{-1}$. Thus, the YOCs appear to have no peculiar motion in the radial direction and co-rotate with the Galactic orbits. The average V_s component of the masers in the Carina Arm is close to that of the young stars, and they may not exhibit lagging motion in relative to Galactic rotation. Contrary to the features in the Perseus and Local Arms, the peculiar motions of the O-type stars in the Carina Arm may be larger than those of the B0–B2-type stars.

The average peculiar motions and std values of the O–B2-types may be larger than those of YOCs or masers in the spiral arms near the Sun. Additionally, in each spiral arm, the B0–B2-type stars perhaps show larger average peculiar motions than the O-type stars. Interestingly, the peculiar motions of sources located in the Perseus and Local Arms may be larger than those in the Carina Arm, implying that the peculiar motions of the young objects at different Galactocentric radii may be different. This issue will be investigated in the next subsection.

Table 3. Average Peculiar Motions of the Sources in the Individual Spiral Arms

Arm	Component	YOCs	O-B2	O	B0-B2	Maser
Perseus	\overline{U}_s (km s ⁻¹)	6.0 ± 2.6	8.8 ± 3.1	-3.8 ± 6.7	13.1 ± 3.1	8.9 ± 2.4
	\overline{V}_s (km s ⁻¹)	-6.5 ± 1.6	-8.5 ± 2.3	-4.0 ± 6.2	-10.0 ± 2.1	-8.0 ± 2.5
	\overline{W}_s (km s ⁻¹)	0.3 ± 0.7	-0.7 ± 0.7	-1.2 ± 2.0	-0.5 ± 0.6	0.7 ± 1.7
	Num	31	51	13	38	28
Local	\overline{U}_s (km s ⁻¹)	1.8 ± 0.7	6.5 ± 1.5	3.1 ± 4.0	7.3 ± 1.5	-0.4 ± 1.8
	\overline{V}_s (km s ⁻¹)	-1.8 ± 0.7	-12.2 ± 2.7	-6.8 ± 6.9	-13.3 ± 2.9	-7.9 ± 1.0
	\overline{W}_s (km s ⁻¹)	0.3 ± 0.3	-0.7 ± 0.7	0.8 ± 1.8	-1.0 ± 0.7	1.8 ± 1.6
	Num	140	52	9	43	28
Carina	\overline{U}_s (km s ⁻¹)	0.3 ± 2.0	-4.8 ± 2.0	-9.0 ± 3.7	-2.6 ± 2.4	3.7 ± 1.7
	\overline{V}_s (km s ⁻¹)	-2.3 ± 1.9	4.5 ± 1.8	-3.3 ± 3.2	8.5 ± 1.9	0.4 ± 1.4
	\overline{W}_s (km s ⁻¹)	0.0 ± 0.8	-1.7 ± 0.5	-1.7 ± 1.1	-1.6 ± 0.6	-4.2 ± 1.2
	Num	35	85	29	56	17

Table 4. Std Values of the Peculiar Motions of Sources in the Individual Spiral Arms

Arm	Component	YOCs	O-B2	O	B0-B2	Maser
Perseus	σ_{U_s} (km s ⁻¹)	14.7	21.8	24.2	19.1	13.0
	σ_{V_s} (km s ⁻¹)	8.8	16.3	22.5	13.2	13.2
	σ_{W_s} (km s ⁻¹)	3.7	4.7	7.0	3.5	9.0
Local	σ_{U_s} (km s ⁻¹)	8.3	10.6	11.9	10.1	9.4
	σ_{V_s} (km s ⁻¹)	8.7	19.5	20.6	19.1	5.5
	σ_{W_s} (km s ⁻¹)	4.1	4.7	5.3	4.5	8.4
Carina	σ_{U_s} (km s ⁻¹)	11.7	18.8	19.9	17.9	6.9
	σ_{V_s} (km s ⁻¹)	11.2	16.4	17.4	14.3	5.8
	σ_{W_s} (km s ⁻¹)	4.9	4.7	5.7	4.1	5.1

3.2. Peculiar Motions Variations along Galactocentric Radius

To study the peculiar motions of the YOCs and O–B2-type stars with respect to Galactocentric radius, we analyze the average peculiar motion as a function of the Galactocentric radius in the range 6–11 kpc, as presented in Figures 5–6. Since sources located in the two spiral arms may have the same Galactocentric distance, we show the average peculiar motions variations along the Galactocentric radius for all sources and sources located in different spiral arms, respectively. Here, the average peculiar motion of each type of sources is calculated within a window of 1 kpc width in steps of 0.25 kpc.

In these figures, the undulations of the peculiar motions of the O–B2-type stars as a function of Galactocentric radius are stronger than those displayed by the YOCs. The U_s component of YOCs may have two “peak”, which are located at $R \sim 7.0$ kpc and $R \sim 9.0$ kpc. However, considering the uncertainties of the values, the peaks are not significant. Thus, more YOCs are needed to further verify them. The U_s component of the O–B2-type stars increases from $R \sim 7.0$ kpc and reaches a maximum of ~ 14 km s $^{-1}$ at a distance of $R \sim 9.0$ kpc. For the V_s components of the YOCs, they show a flat distribution from 6.0 to 9.0 kpc, and decrease beyond 9.0 kpc. For the V_s components of the O–B2-type stars, they decline from 7.0 to 8.5 kpc and reach minimum of ~ -12 km s $^{-1}$ at a distance of $R \sim 8.5$ kpc. Outside 7.5 kpc, the V_s component of the YOCs and O–B2-type stars remain smaller than zero, indicating the young objects may rotate slower than Galactic rotation. The YOCs are more massive than single O–B2-type stars and would therefore better represent the average motion. Their declining V_s velocity as a function of radius beyond 9.0 kpc could also suggest that the assumed rotation curve may overestimate the rotation velocity of the Milky Way. As for the W_s components of the YOCs and O–B2-type stars, their undulations are both weak and do not exceed ± 2 km s $^{-1}$ in the Galactocentric range of 6–11 kpc.

In the Perseus Arm, the U_s components appear to decrease with the Galactocentric radius for both YOCs and O–B2-type stars. The V_s components of YOCs appear to decrease with Galactocentric radius, but increase with the radius for the O–B2-type stars. In the Local Arm, both the U_s and V_s components appear to show a “U” structure along the Galactocentric radius for YOCs and O–B2-type stars. The lowest point of “U” structure is at about 8.0 kpc. In the Carina Arm, the U_s components of YOCs and O–B2-type stars appear to increase as the Galactocentric radius and would pass through the zero point at 7.0–7.5 kpc. The V_s components of YOCs and O–B2-type stars do not appear to fluctuate significantly with the Galactocentric radius.

Between 7.0 and 8.0 kpc, the sources located in the Carina Arm and the Local Arm may have the same Galactocentric radius. We further investigate the kinematic features of sources located in different spiral arms while having the same Galactocentric radius. The U_s components decrease in this range for sources located in the Local Arm, while they increase for sources located in the Carina Arm. They would intersect at around 7.5 kpc. The V_s components of the YOCs located in the Local Arm are larger than those in the Carina Arm. O–B2-type stars seem to exhibit the opposite phenomenon of YOCs. Both young objects indicate that the kinematic features may be different for the sources located in the two arms, while it needs to be confirmed with more young stars.

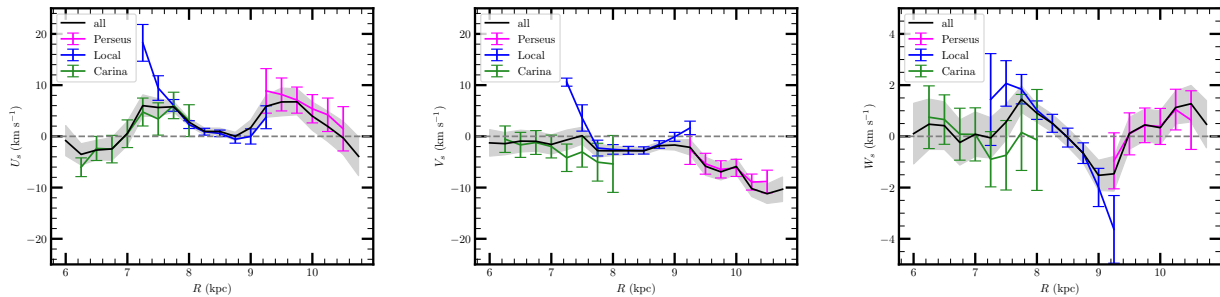


Figure 5. The average peculiar motions of the YOCs as a function of Galactocentric distance, R . The black solid lines indicate all sources, and shaded area represent the uncertainties. The magenta, blue, and green lines represent the sources located in the Perseus, Local, and Carina Arms. The average is calculated within a window of 1 kpc width in steps of 0.25 kpc, and R_0 is 8.15 kpc. Each interval must have more than five sources.

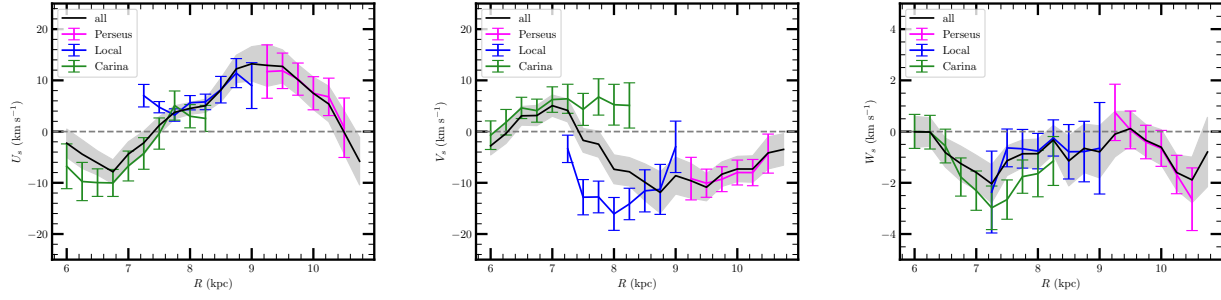


Figure 6. The average peculiar motions of the O–B2-type stars as a function of Galactocentric distance, R . The others are the same as Figure 5.

4. KINEMATIC DISTANCE

Traditionally, one can construct a simple model of the rotation speeds of sources as a function of distance from the center of the Milky Way. Then, if one measures the line-of-sight velocity (radial velocity) of an object, one can determine its distance by matching the observation with the model prediction, which yields a kinematic distance. However, the distances of sources derived from kinematic methods may be unreliable due to noncircular (peculiar) motions. The significant peculiar motions of the sources are expected to affect their estimated kinematic distance. [Xu et al. \(2006\)](#) found a parallax distance of 1.95 ± 0.04 kpc of the high-mass star-forming region W3(OH). The kinematic distance (i.e., > 4 kpc) was more than twice as far as the parallax distance. Hence, it is crucial to correct the kinematic model in regions where the peculiar motions of sources are prominent to obtain relatively precise kinematic distance estimations.

First, we convert the heliocentric radial velocities of the YOCs and O–B2-type stars to the local standard of rest (LSR) velocities. The solar motion values derived from stars in different evolutionary stages are different ([Binney & Tremaine 2008](#)). Since the objects discussed here are mainly young stars, we do not use the IAU solar motion. Instead, we use a “revised LSR velocity” (V_{LSR}) by applying the updated solar motion values obtained from masers ([Reid et al. 2019](#)) to estimate the kinematic distance of each object, which can be calculated by

$$V_{\text{LSR}} = V_{\text{Helio}} + (V_{\odot} \sin l + U_{\odot} \cos l) \cos b + W_{\odot} \sin b, \quad (1)$$

where V_{Helio} is the heliocentric radial velocity, l and b are the Galactic longitude and latitude, and U_{\odot} , V_{\odot} , and W_{\odot} are the solar motions. For a source with a given Galactic longitude and distance from the Sun, we can calculate its circular motion, Θ , in the Galactic plane using the universal rotation curve ([Persic et al. 1996](#); [Reid et al. 2019](#)).

The radial velocity of a source is the key to determining its kinematic distance. Here, we define an assumed LSR radial velocity in a pure Galactic circular orbit, $V_{\text{LSR}}^{\text{mod}}$, which can be calculated by

$$V_{\text{LSR}}^{\text{mod}} = (\Theta(r) \cos \gamma - \Theta(R_0) \sin l) * \cos b, \quad (2)$$

where $\Theta(r)$ is the theoretical rotation velocity at Galactocentric radius r calculated by using the rotation curve. γ is the angle between the line-of-sight direction and the rotation direction of the source, and $R_0 = 8.15$ kpc ([Reid et al. 2019](#)). A schematic depiction of these parameters is given in Figure 7. In contrast, if we know the LSR velocity of a source, its kinematic distance, d , can be derived by Equation (2).

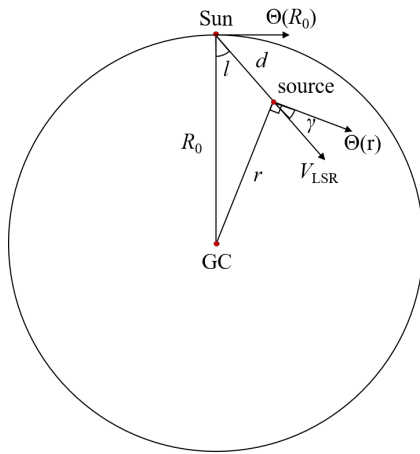


Figure 7. Schematic depiction of the source and Galactic parameters.

We adopt the probability density function (PDF, P) to estimate the kinematic distance. Following [Reid et al. \(2016\)](#), we calculate it via

$$P = \frac{1 - \exp[-(\Delta V_{\text{LSR}}/\sigma_{V_{\text{LSR}}})^2/2]}{(\Delta V_{\text{LSR}}/\sigma_{V_{\text{LSR}}})^2/2}, \quad (3)$$

where ΔV_{LSR} is the difference between the LSR velocity and that expected from the rotation model of the Galaxy, $\sigma_{V_{\text{LSR}}}$ is the uncertainty of the LSR velocity. Uncertainties in the kinematic distances include the 1σ width of the PDF

and uncertainties caused by the parameters in the rotation curve, i.e., a_2 (0.96 ± 0.05) and a_3 (1.62 ± 0.02 , Reid et al. 2019).

Figure 8 (a) presents the distributions of YOCs, O–B2-type stars, and masers in a longitude–velocity (l – v) diagram. Since YOCs and O–B2-type stars are mainly located within 6 kpc from the Sun, only masers in this range are selected for comparison. The distributions of the YOCs and O–B2-type stars are roughly consistent with that of the masers in the l – v diagram, although they all have large dispersions. We calculate the average LSR radial velocities of the masers, YOCs, and O–B2-type stars with a Galactic longitude step every 20° , as shown Figure 8 (b). Overall, the LSR velocities of the three young populations are concordant in most locations. Near the Galactic longitude of 30° , the large differences in the LSR velocities among the three groups may be due to a lack of YOCs and O–B2-type stars (see Figure 8 (a)). Therefore, we can combine the YOCs and O–B2-type stars to revise the model of kinematic distance estimation.

In Figure 9, we display the distributions of the three spiral arms near the Sun in the l – v diagram and of the YOCs and O–B2-type stars located within 1σ from the centers of the spiral arms in the Galactic plane for comparison. Here, the spiral arms are from the model presented by Xu et al. (2023), and $V_{\text{LSR}}^{\text{mod}}$ of each spiral arm is calculated using Equation (2). In the l – v diagram, the selected YOCs and O–B2-type stars are expected located near the spiral arms, while there are significant and systematic discrepancies between their measured V_{LSR} (using Equation (1), shown as the colored points in Figure 9) and $V_{\text{LSR}}^{\text{mod}}$ values (the colored lines in Figure 9). It is caused by the peculiar motion of sources. This suggests that the kinematic distances of these objects directly obtained from radial velocities deviate from their parallax distances. Therefore, in order to obtain more reliable kinematic distances for these sources, one can consider deducting the peculiar motions by adding offsets to radial velocities during the estimation.

Considering that the amount of YOCs and O–B2-type stars is limited and that they are mainly concentrated in spiral arms, we focus on correcting the kinematic distance model toward the regions where the LSR velocity discrepancies between the sources and spiral arms are significant. For example, near the direction of $l \sim 60^\circ - 90^\circ$ in the Local Arm, sources with LSR velocities less than -10 km s^{-1} have significant discrepancies between V_{LSR} and $V_{\text{LSR}}^{\text{mod}}$, as shown in Figure 9. After an offset of approximately 28 km s^{-1} is applied to those sources, their distributions are close to the Local Arm in the l – v diagram. Hence, this offset can yield more reliable kinematic distance estimations for these sources. In total, six regions are found to need compensation via LSR velocity offsets for accurate kinematic distance estimations (see the expected values of these offsets in Table 5). Although the offsets are determined using sources in the spiral arms, in practice, it is not necessary to consider whether the source is located in a spiral arm, but only the conditions listed in Table 5, i.e., Galactic longitude and radial velocity.

The offsets are derived from the YOCs and O–B2-type stars located within 1σ from the center of the spiral arms in the Galactic plane. Then we apply them to all young objects that meet the criteria in Table 5. The parallax distances, standard distances, and revised distances of the YOCs and O–B2-type stars are presented in Figure 10(a). Here, the standard kinematic distances are estimated without considering peculiar motion, while the revised kinematic distances are obtained by adding the offsets listed in Table 5 to counteract the peculiar motion. For the YOCs and O–B2-type stars, their standard kinematic distances are generally greater than their parallax distances, while their revised kinematic distances are closer to their parallax distances. Moreover, we divide the YOCs and O–B2-type stars randomly into two groups, and calculate the standard kinematic distances for one group and the revised kinematic distances for the other group. After 100 re-samples and repetitions of the experiment, the average median value of the offset between standard kinematic distance and the parallax distance is 2.2 kpc, and average dispersion is 1.6 kpc. The corresponding values for the revised kinematic distance and parallax distance are 0.2 and 1.9 kpc, respectively. The typical relative uncertainty of the kinematic distance for these young objects is about 0.3. Furthermore, for the offsets in correction that are listed in Table 5, we check them using the masers, since their distribution are consistent with those of the YOCs and O–B2-type stars in the l – v diagram (Figure 8). As shown in Figure 10(b), compared with the standard kinematic distances, the revised kinematic distances of the masers are in agreement with their parallax distances, and the median offset is reduced from 2.0 to 0.3 kpc. The offsets, which are obtained from a fraction of YOCs and O–B2-type stars, are successfully applied not only all YOCs and O–B2-type stars, but also masers. It suggests that the method adopted here is effective.

The above results indicates that, within the range of 6 kpc from the Sun, if a source satisfies the conditions listed in Table 5, one can add the corresponding offset to its observed radial velocity to determine a more reliable kinematic distance than the standard kinematic distance. However, using the present-day data, we can make kinematic distance correction in only six regions in the solar neighborhood. With an increase of available data in the future, we are

expected to modify the kinematic distance model in all regions near the Sun, and even in the distant regions of the Milky Way.

5. SUMMARY

We investigate the kinematics of YOCs and O–B2-type stars in the local spiral structure. The YOCs and O–B2-type stars in the different spiral arms show different kinematic features. The young populations located in the outer spiral arms may exhibit larger peculiar motions than those in the inner spiral arms. In the Perseus and Local Arms, the YOCs and O–B2-type stars perhaps move towards the GC and rotate slower than the rotation of the Milky Way. In contrast, the young populations in the Carina Arm may move toward the Galactic anticenter and rotate slightly faster of Galactic rotation. Using the astrometric parameters of the young stellar populations, we also perform kinematic distance corrections for several regions in the solar neighborhood. At present, the corrections to the kinematic distance estimates are only valid up to 6 kpc from the Sun, yet it provides a useful reference for future kinematic distance estimates.

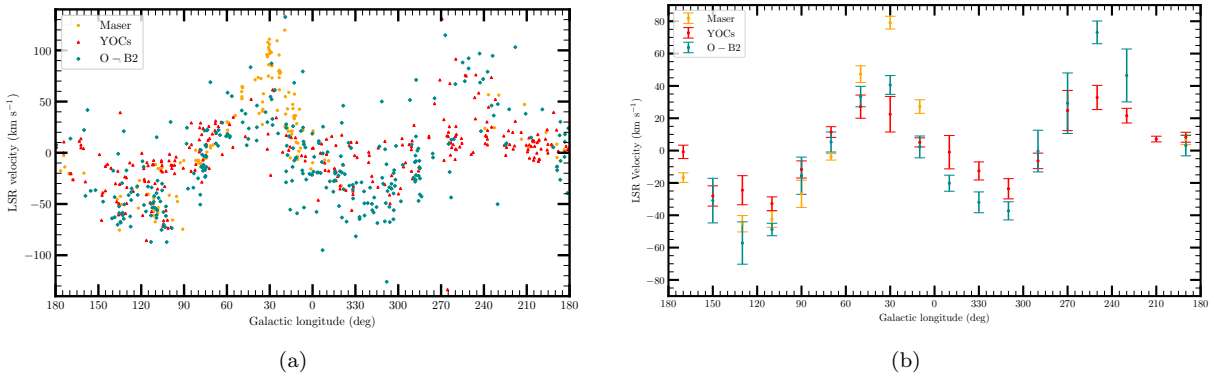


Figure 8. (a): l – v diagram. Colored dots are the sources of masers (orange dots), YOCs (red triangles), and O–B2-type stars (cyan diamonds). (b): variations in the average V_{LSR} per 20° for the masers (orange), YOCs (red), O–B2-type stars (cyan) along Galactic longitude. Each interval must have more than five sources.

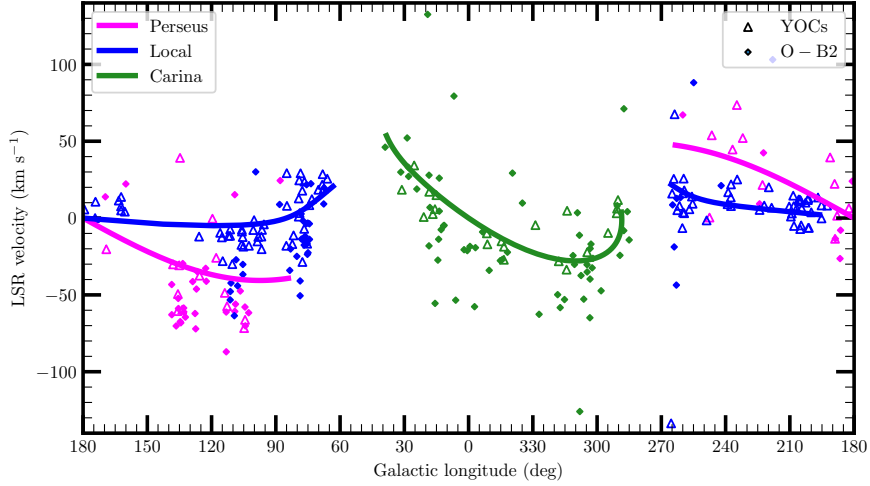


Figure 9. V_{LSR} values of the YOCs (triangles) and O–B2-type stars (diamonds) being assigned to the corresponding spiral arms (lines) as a function of Galactic longitude. The magenta, blue, and green lines represent the Perseus Arm, the Local Arm, and the Carina Arm, respectively, whose $V_{\text{LSR}}^{\text{mod}}$ values are calculated by using Equation (2).

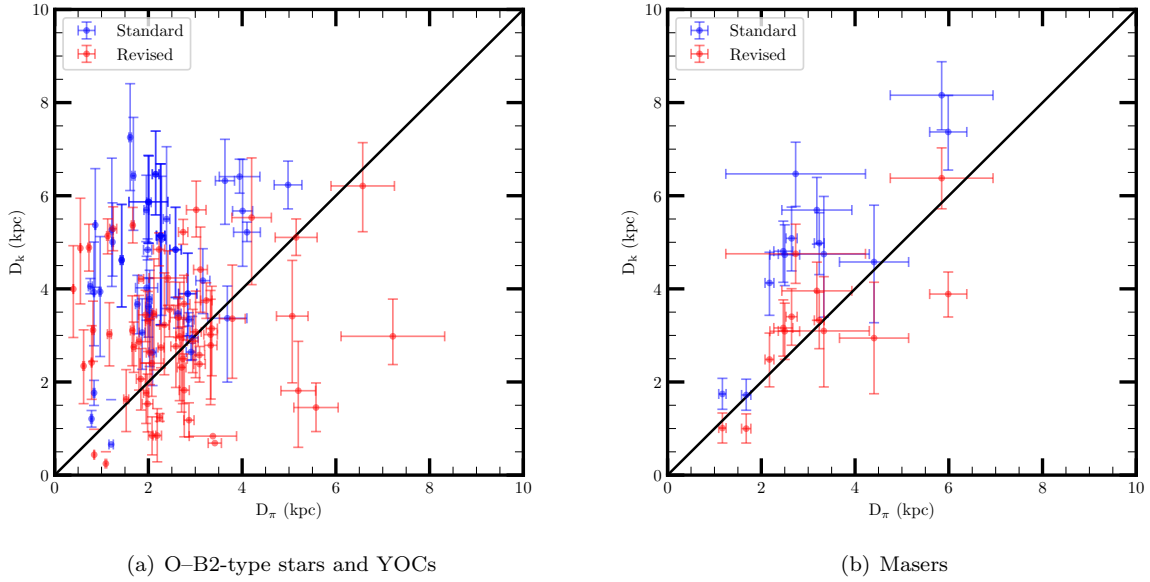


Figure 10. Comparison between the parallax and kinematic distances. The young stellar population is shown in the left panel, and the masers are shown in the right panel. D_π is the distance converted from the measured parallax. D_k is the kinematic distance. The standard kinematic distance is obtained without considering the peculiar motion. The revised kinematic distance is obtained by adding the offsets to radial velocity to counteract the peculiar motion.

Table 5. Offsets Used for the Kinematic Distance Estimation

l ($^\circ$)	condition	offset (km s^{-1})
60–90	$V_{\text{LSR}} < -10 \text{ km s}^{-1}$	28
90–130	$V_{\text{LSR}} < -45 \text{ km s}^{-1}$	20
130–150	$V_{\text{LSR}} < -50 \text{ km s}^{-1}$	27
230–250	$V_{\text{LSR}} > 50 \text{ km s}^{-1}$	–10
250–280	$V_{\text{LSR}} < 0 \text{ km s}^{-1}$	30
290–330	$V_{\text{LSR}} < -40 \text{ km s}^{-1}$	25

We appreciate the anonymous referee for the instructive comments that helped us to improve the paper. This work was funded by the NSFC Grants 11933011, National SKA Program of China (Grant No. 2022SKA0120103) and the Key Laboratory for Radio Astronomy. L.Y.J. thanks the support of the NSFC grant No. 12203104, the Natural Science Foundation of Jiangsu Province (grant No. BK20210999). This work has made use of data from the European Space Agency (ESA) mission *Gaia* (<https://www.cosmos.esa.int/gaia>) processed by the *Gaia* Data Processing and Analysis Consortium (DPAC, <https://www.cosmos.esa.int/web/gaia/dpac/consortium>). Funding for the DPAC has been provided by national institutions, in particular the institutions participating in the *Gaia* Multilateral Agreement.

REFERENCES

- Bian, S. B., Xu, Y., Li, J. J., et al. 2022, *AJ*, 163, 54, doi: [10.3847/1538-3881/ac3d90](https://doi.org/10.3847/1538-3881/ac3d90)
- Binney, J., & Tremaine, S. 2008, *Galactic Dynamics: Second Edition* (Princeton University Press)
- Brunthaler, A., Reid, M. J., Menten, K. M., et al. 2011, *AN*, 332, 461, doi: [10.1002/asna.201111560](https://doi.org/10.1002/asna.201111560)
- Castro-Ginard, A., Jordi, C., Luri, X., et al. 2022, *A&A*, 661, A118, doi: [10.1051/0004-6361/202142568](https://doi.org/10.1051/0004-6361/202142568)
- Chen, Y., Zhou, P., & Chu, Y.-H. 2013, *ApJL*, 769, L16, doi: [10.1088/2041-8205/769/1/L16](https://doi.org/10.1088/2041-8205/769/1/L16)
- Dame, T. M., Hartmann, D., & Thaddeus, P. 2001, *ApJ*, 547, 792, doi: [10.1086/318388](https://doi.org/10.1086/318388)
- Dias, W. S., Monteiro, H., Lépine, J. R. D., & Barros, D. A. 2019, *MNRAS*, 486, 5726, doi: [10.1093/mnras/stz1196](https://doi.org/10.1093/mnras/stz1196)
- Fabricius, C., Luri, X., Arenou, F., et al. 2021, *A&A*, 649, A5, doi: [10.1051/0004-6361/202039834](https://doi.org/10.1051/0004-6361/202039834)
- Gaia Collaboration, Brown, A. G. A., Vallenari, A., et al. 2018a, *A&A*, 616, A1, doi: [10.1051/0004-6361/201833051](https://doi.org/10.1051/0004-6361/201833051)
- Gaia Collaboration, Katz, D., Antoja, T., et al. 2018b, *A&A*, 616, A11, doi: [10.1051/0004-6361/201832865](https://doi.org/10.1051/0004-6361/201832865)
- Gaia Collaboration, Brown, A. G. A., Vallenari, A., et al. 2021, *A&A*, 649, A1, doi: [10.1051/0004-6361/202039657](https://doi.org/10.1051/0004-6361/202039657)
- Gaia Collaboration, Drimmel, R., Romero-Gomez, M., et al. 2022a, arXiv e-prints, arXiv:2206.06207, doi: [10.48550/arXiv.2206.06207](https://doi.org/10.48550/arXiv.2206.06207)
- Gaia Collaboration, Vallenari, A., Brown, A. G. A., et al. 2022b, arXiv e-prints, arXiv:2208.00211, doi: [10.48550/arXiv.2208.00211](https://doi.org/10.48550/arXiv.2208.00211)
- Georgelin, Y. M., & Georgelin, Y. P. 1976, *A&A*, 49, 57
- Hao, C. J., Xu, Y., Wu, Z. Y., et al. 2022a, *A&A*, 668, A13, doi: [10.1051/0004-6361/202244570](https://doi.org/10.1051/0004-6361/202244570)
- . 2022b, *A&A*, 660, A4, doi: [10.1051/0004-6361/202243091](https://doi.org/10.1051/0004-6361/202243091)
- Hao, C. J., Xu, Y., Hou, L. G., et al. 2021, *A&A*, 652, A102, doi: [10.1051/0004-6361/202140608](https://doi.org/10.1051/0004-6361/202140608)
- Hou, L. G., & Han, J. L. 2014, *A&A*, 569, A125, doi: [10.1051/0004-6361/201424039](https://doi.org/10.1051/0004-6361/201424039)
- Immer, K., Li, J., Quiroga-Nuñez, L. H., et al. 2019, *A&A*, 632, A123, doi: [10.1051/0004-6361/201834208](https://doi.org/10.1051/0004-6361/201834208)
- Immer, K., & Rygl, K. L. J. 2022, *Universe*, 8, 390, doi: [10.3390/universe8080390](https://doi.org/10.3390/universe8080390)
- Lindegren, L., Bastian, U., Biermann, M., et al. 2021, *A&A*, 649, A4, doi: [10.1051/0004-6361/202039653](https://doi.org/10.1051/0004-6361/202039653)
- Persic, M., Salucci, P., & Stel, F. 1996, *MNRAS*, 281, 27, doi: [10.1093/mnras/278.1.27](https://doi.org/10.1093/mnras/278.1.27)
- Qin, S., Zhong, J., Tang, T., & Chen, L. 2023, *ApJS*, 265, 12, doi: [10.3847/1538-4365/acadd6](https://doi.org/10.3847/1538-4365/acadd6)
- Reid, M. J., Dame, T. M., Menten, K. M., & Brunthaler, A. 2016, *ApJ*, 823, 77, doi: [10.3847/0004-637X/823/2/77](https://doi.org/10.3847/0004-637X/823/2/77)
- Reid, M. J., Menten, K. M., Zheng, X. W., et al. 2009, *ApJ*, 700, 137, doi: [10.1088/0004-637X/700/1/137](https://doi.org/10.1088/0004-637X/700/1/137)
- Reid, M. J., Menten, K. M., Brunthaler, A., et al. 2014, *ApJ*, 783, 130, doi: [10.1088/0004-637X/783/2/130](https://doi.org/10.1088/0004-637X/783/2/130)
- . 2019, *ApJ*, 885, 131, doi: [10.3847/1538-4357/ab4a11](https://doi.org/10.3847/1538-4357/ab4a11)
- Sakai, N., Reid, M. J., Menten, K. M., Brunthaler, A., & Dame, T. M. 2019, *ApJ*, 876, 30, doi: [10.3847/1538-4357/ab12e0](https://doi.org/10.3847/1538-4357/ab12e0)
- Soubiran, C., Cantat-Gaudin, T., Romero-Gómez, M., et al. 2018, *A&A*, 619, A155, doi: [10.1051/0004-6361/201834020](https://doi.org/10.1051/0004-6361/201834020)
- VERA Collaboration, Hirota, T., Nagayama, T., et al. 2020, *PASJ*, 72, 50, doi: [10.1093/pasj/psaa018](https://doi.org/10.1093/pasj/psaa018)
- Xu, Y., Hao, C. J., Liu, D. J., et al. 2023, *ApJ*, 947, 54, doi: [10.3847/1538-4357/acc45c](https://doi.org/10.3847/1538-4357/acc45c)
- Xu, Y., Hou, L. G., Bian, S. B., et al. 2021, *A&A*, 645, L8, doi: [10.1051/0004-6361/202040103](https://doi.org/10.1051/0004-6361/202040103)
- Xu, Y., Reid, M. J., Zheng, X. W., & Menten, K. M. 2006, *Science*, 311, 54, doi: [10.1126/science.1120914](https://doi.org/10.1126/science.1120914)
- Xu, Y., Li, J. J., Reid, M. J., et al. 2013, *ApJ*, 769, 15, doi: [10.1088/0004-637X/769/1/15](https://doi.org/10.1088/0004-637X/769/1/15)
- Xu, Y., Bian, S. B., Reid, M. J., et al. 2018, *A&A*, 616, L15, doi: [10.1051/0004-6361/201833407](https://doi.org/10.1051/0004-6361/201833407)
- Zhang, B., Reid, M. J., Zhang, L., et al. 2019, *AJ*, 157, 200, doi: [10.3847/1538-3881/ab141d](https://doi.org/10.3847/1538-3881/ab141d)